Helmholtz-Zentrum
Geesthacht
Zentrum für Material- und Küstenforschung

Final Draft
of the original manuscript:

Yu, Z.J.; Huang, Y.; Qiu, X.; Yang, Q.; Sun, W.; Tian, Z.;
Zhang, D.P.; Meng, J.:

Fabrication of magnesium alloy with high strength and heat-resistance by hot extrusion and ageing

In: Materials Science and Engineering A (2013) Elsevier

DOI: 10.1016/j.msea.2013.04.108

Fabrication of magnesium alloy with high strength and heat-resistance by hot extrusion and ageing

Z. J. Yu[a,c], Yuanding. Huang[b], X. Qiu[a], Q. Yang[a], W. Sun[a], Z. Tian[a], D. P. Zhang[a] and J. Meng[a*]

a. *State Key Laboratory of Rare Earth Resources Utilization, Changchun Institute of Applied Chemistry, Chinese Academy of Sciences, Changchun 130022, People's Republic of China*

b. *MagIC-Magnesium Innovation Centre, Helmholtz-Zentrum Geesthacht, Max-Planck-Str. 1, D-21502 Geesthacht, Germany*

c. *University of Chinese Academy of Sciences, Beijing 100049, P. R. China*

Abstract

A Mg-11Gd-4.5Y-1.5Zn-1Nd-0.5Zr alloy with high-strength and heat-resistance has successfully been prepared by hot extrusion and subsequent ageing. It exhibits an ultimate tensile strength of 473 MPa, 0.2% proof stress of 373 MPa and elongation to failure of 4.1% at room temperature. At 250 °C, this alloy shows an ultimate tensile strength of 369 MPa, 0.2% proof stress of 316 MPa and elongation to failure of 6.3%. Its good mechanical properties and thermal stability are attributed to the dispersion of large volume fraction of 14H-LPSO phase, small α-Mg grains, basal-fiber texture and dense distribution of precipitates at the grain boundaries and inside the grains.

Keywords: Mg-Gd-Y-Zn-Nd-Zr alloy; heat resistance; hot-extrusion; ageing

*Corresponding author. Tel: +86-431 85262030; fax: +86-431 85698041

E-mail address: jmeng@ciac.jl.cn (J. Meng)

1. Introduction

Mg-Gd alloys receive significant attention due to the combination of high strength and ductility. These alloys are developed for both elevated temperature and bio-implant applications [1, 2]. Due to a large solubility of Gd in Mg, it is possible to adjust the mechanical properties of these alloys by thermo-mechanical treatments [3–10]. The precipitation sequence in Mg-Gd alloys is well known [11]:

$$\beta'' \rightarrow \beta' \rightarrow \beta_1 \rightarrow \beta$$

The precipitation of metastable β' phase contributes to the maximum hardening during age. The LPSO (Long-Period Stacking Order) phases form with the addition of Zn to Mg-Gd(-Y) alloys [7], which provides an additional contribution to strengthening. By optimizing the microstructure through the control of deformation processes, such as warm rolling and hot extrusion, and the subsequent annealing process, a mechanical properties with high strength at room temperature and good creep resistance can be achieved for these Mg-Gd alloys [3–10].

The addition of Nd in Mg-Gd alloys reduces the solubility of Gd in magnesium, and promotes the precipitation of β' phase. Negishi et al. added Nd into the binary Mg-Gd alloys to prepare Mg-Gd-Nd alloys [12]. They found that Mg-3Gd-3Nd (wt.%) alloy exhibited a enhanced age-hardening response even at 250 °C compared to the binary Mg-Gd. The creep resistance of Mg-6Gd-3Nd (wt.%) alloy was even better than that of commercial magnesium alloy WE54 at 250 °C [12]. Compared with Gd, the price of Nd is lower.

By optimizing the thermo-mechanical process, i.e. hot extrusion followed by ageing treatment, Homma et al. successfully prepared a Mg-Gd-Y-Zn-Zr alloy with excellent

mechanical properties at room temperature [10]. This alloy has a ultimate tensile strength (UTS) up to 542 MPa, a yield strength (YS) up to 473 MPa and an elongation to failure up to 8%. The high strength is attributed to the precipitation of fine metastable β' phase and LPSO phase. Many Mg-RE-Zn (RE-rare earths) alloys exhibit an outstanding mechanical properties due to the existence of LPSO phase in their matrix [10, 13–16], indicating that the LPSO phase has a large strengthening effect on the matrix. The strengthening mechanism of magnesium alloys containing the LPSO-phase has not yet been clarified. Recently, Hagihara et al. [17, 18] demonstrated that the plastic deformation of LPSO phase is highly anisotropic. In the LPSO phase, the (0001) $<11\bar{2}0>$ basal slip is the dominant deformation mode at room temperature. Hagihara et al. suggested that the plastic anisotropy of the LPSO phase could be used to strengthen the mechanical properties of Mg alloys according to the positional relationship between the LPSO phase and the load direction. Up to now, much attentions have been paid to the strengthening mechanism of LPSO phase at room temperature and its structural features. However, its influences on the thermal stability of microstructure are rarely reported.

In this paper, an investigation on Mg-11Gd-4.5Y-1.5Zn-1Nd-0.5Zr alloy with high-strength and heat-resistance prepared by hot extrusion and subsequent ageing process is reported. The influence of LPSO and other phases on the thermal stability of microstructure as well as the strengthening mechanism of LPSO phases are discussed. The present work considers the effect of addition of Nd into Mg-Gd-Y-Zn-Zr alloy. The relationship between mechanical properties and microstructure of this alloy is presented and investigated.

2. Experimental procedures

The investigated alloy is Mg-11Gd-4.5Y-1.5Zn-1Nd-0.5Zr (weight percent) was prepared by melting pure Mg and Zn at 750 °C in an electric resistance furnace under a mixed atmosphere of carbon dioxide and sulfur hexafluoride. The additions of other elements were carried out using Mg-20Gd (wt. %), Mg-20Y (wt. %), Mg-20Nd (wt. %) and Mg-30Zr (wt. %) master alloys. After melting and stirring, the melt was poured into a water-cooled cylindrical iron mold with a diameter of 90 mm at 720 °C. The homogenization annealing of this cylindrical billet was performed at 535 °C for 24 hours followed by air cooling (T4 treatment). The homogenized billet was then machined into the round bars with a diameter of 82 mm for the subsequent extrusion. These bars were preheated at 410 °C for 2 hours, and then extruded at the same temperature with an extrusion ratio of 13:1. A sheet with a width of 50 mm and a thickness of 8 mm was obtained after extrusion. The extruded sheet was further aged at 200 °C for 72 hours followed by air cooling (T5 treatment).

The tensile specimens with a gauge length of 25 mm, width 4 mm and thickness 2 mm were prepared from the extruded sheet by electro discharge cutting. The tensile tests were carried out on a uni-axial tensile testing machine equipped with an induction heating furnace at a cross-head speed of 1 mm/min. The test temperatures are 25 °C, 200 °C, 250 °C, 300 °C.

The texture of the samples was determined by electron backscattered diffraction (EBSD) with a step size of 0.5 μm on a FEI Nova 400 with a HKL-EBSD system. In order to investigate the influence of temperature on the stability of grain size, the extruded samples were annealed at 400 °C and 450 °C for 72 hours in a resistance

heating furnace. Their microstructures were observed using optical microscopy (OM) and scanning electron microscopy (SEM). The chemical compositions of particles were analyzed by energy dispersive spectroscopy (EDS). The average grain size was measured using liner intercept method. The precipitate microstructures were observed with transmission electron microscopy (TEM). The foils for TEM observations were prepared using a Gatan ion beam thinning machine (Milling parameters: Ar, 5 kv, 25 °C, 40 min). The second phases were identified by X-ray diffraction (XRD) (D8 FOCUS X-ray diffractometer) with Cu K_α radiation.

3. Results

3.1 Microstructures of the as-cast and extruded samples with and without heat treatments

Fig. 1 shows the X-ray diffraction (XRD) patterns of the alloy investigated following various processing conditions. The as-cast sample contains α-Mg solid solution, Mg_5RE, Mg_3RE and $Mg_{12}REZn$ phases (RE includes Gd, Y, Nd). After T4 treatment both the Mg_5RE and Mg_3RE phases are not detected, but $Mg_{12}REZn$ phase is present. The amount of the $Mg_{12}REZn$ increases due to that the intensities of its corresponding peaks increase. The sample after T4 homogenization treatment mainly consist of α-Mg and $Mg_{12}REZn$.

The XRD patterns of the as-extruded samples with and without annealing treatments are shown in Fig. 2. The as-extruded sample contains α-Mg and Mg_5RE phases, while Mg_3RE phase could not be observed (Fig. 2a). Mg_5RE phase seems to have re-precipitated during the subsequent extrusion process. For the extruded sample with following ageing to peak hardening at 200 °C for 72 h. (Fig. 2b), only the Mg_5RE and α-Mg are identified from the XRD profiles. The present XRD could not detect the peaks of β' phase. The reasons are unclear at moment. Maybe, the diffraction peaks of

β' phase are overlapped with that from other phases, especially with peaks from Mg because β' phase is normally completely coherent with Mg matrix. Another reason is possible due to the fact that β' phase has a very small size in nanometer order. The further investigations on the precipitates (β' phases) forms during ageing treatment will be carried on by TEM. After annealing at a higher temperature 400 °C, the $Mg_{12}REZn$ phase is observed in addition to the Mg_5RE phase. Increasing in the annealing temperature to 450 °C, the Mg_5RE observed in the as-extruded alloy dissolves and the $Mg_{12}REZn$ phase forms.

Fig. 3a and d show the microstructures of the as-cast alloy and the T4 treated alloy. The as-cast alloy is mainly composed of rosette-shaped dendrites. According to the XRD results (Fig. 1a), the main precipitates in the as-cast alloy consist of $Mg_{12}REZn$, Mg_5RE and Mg_3RE phases. These phases are distributed in the interdendritic regions (Fig. 3a). After the T4 treatment, only $Mg_{12}REZn$ phase is detected with XRD (Fig. 1b). The rod-like precipitates (marked by white arrows) are found in both the as-cast and the T4 treated samples, but most eutectic precipitates (marked by black arrows) disappear in the T4 treated sample. This indicates that eutectic precipitate is the Mg_3RE and/or Mg_5RE phases, while the rod-like precipitate is $Mg_{12}REZn$ phase. The corresponding EDS analysis results are showed in Fig. 4 and are discussed in the following paragraphs. The optical microstructures of the as-extruded sheet with and without annealing are showed in Fig. 3c-e. The grains gradually coarsen after annealing at 400 °C or 450 °C for 72 hours (Fig. 3d and e) ,but the growth rate is very low as the average grain size is still ~4 μm and ~8 μm after annealing at 400 °C and 450 °C for 72 hours, respectively. This demonstrates that the refined microstructure of the extruded sheet is thermal stable. In Fig. 3c, d and e,

the rod-like shaped particles (marked by white arrows) located at the grain boundaries are parallel to ED. A large number of irregular particles (marked by black arrow) form at the grain boundaries during hot extrusion due to dynamic precipitation, while most of them dissolve into matrix during annealing treatment and residual one coarsen.

Fig. 4 shows the SEM images and EDS analysis of precipitates existed in the samples at different processes including casting, hot extrusion and annealing. In the as-cast sample (Fig. 4a), three different precipitates are detected, which are marked as A, B and C. The precipitate A has a Mg concentration of 76.46 at.%, a rare earth concentration of 13.09 at.% and a Zn concentration of 6.93 at.%, respectively. The Mg content of equilibrium phase Mg_3RE is expected to be 75 at.%. Thus, the precipitate A is identified as Mg_3RE or possibly Mg_3(RE, Zn) phases. The precipitate B has a chemical composition of 80.34 at.% Mg, 13.88 at.% RE and 5.73 at.% Zn. These values are consistent with the stoichiometry of equilibrium phase Mg_5RE phase. The compositions of rod-like precipitate (marked as C) is 89.05 at.% Mg and 2.96 at.% Zn. The total concentration of rare earth elements is approximately 7.69 at.%. The rod-like precipitates with similar chemical compositions also exist in the cast-T4, as-extruded, extruded-T5 and annealed samples (marked as E, G, I and K in Fig. 4 b-e). Considering the corresponding EDS results, their stoichiometry is close to that of $Mg_{12}REZn$ phase.

In the cast-T4 sample (Fig. 4b), besides $Mg_{12}REZn$ phase, another precipitate marked as D is found. Since the precipitate D has a similar shape and chemical composition as the precipitate B in the as-cast sample, it is determined to be approximately Mg_5RE phase, which did not fully dissolve into the matrix during T4 process. The Mg_3RE phases cannot be detected in this sample. In the as-extruded and extruded-T5 samples (Fig. 4c and d),

the irregular precipitates (marked as F and H) have a smaller size, but a higher amount. Its chemical composition is Mg94.33RE6.24Zn3.15 (at.%) in the as-extruded sample and Mg88.99RE7.47Zn3.53 (at.%) in the extruded-T5 sample, respectively. Due to their small size, the EDS results are influenced by the Mg matrix, thus they have a higher Mg content over 94 at%. According to the XRD and TEM results in the other sections, these particles are Mg_5RE formed during the hot-extrusion processing. After annealing treatment at 450 °C for 72 h (Fig. 4e), a small amount of precipitate J still exist around the grain boundaries. Although the precipitate J coarsen obviously, its chemical composition of Mg88.59RE10.23Zn1.18 (at.%) is close to Mg_5RE phase. Compared with as-extruded and extruded-T5 samples, the number of Mg_5RE phases in the annealed sample (Fig. 4e) sharply decrease, while their sizes increase. However, the annealing treatment has less influence on the number and morphology of $Mg_{12}REZn$ phases, which are marked in the Fig. 4.

Fig. 5a shows the inverse pole figure (IPF) of the as-extruded alloy with the observation direction parallel to the transverse direction (TD). The regions with green contrasts in the IPF correspond to the rod-like precipitates and Mg_5RE phases that could not be identified. As shown in Fig. 5, the dynamic recrystallization occur in the α-Mg matrix during hot extrusion. The recrystallized grains have an average grain size of ~2.5 μm. Fig. 5b shows a typical extrusion texture with the $[10\bar{1}0]$ direction of most recrystallized grains parallel to the extrusion direction (ED). The highest intensity at $[10\bar{1}0]$ is much larger than that at $[11\bar{2}0]$. A second texture peak at approximately $[11\bar{2}1]$ parallel to the extrusion direction is also shown in Fig. 5b. However, this second peak is less intense than the main extrusion texture component at $[10\bar{1}0]$. Basal planes of most

grains are parallel to the ED-TD plane and $\{10\bar{1}0\}$ prismatic planes parallel to the transversal direction [20, 21].

Further observations on the microstructures of as-extruded and peak-aged samples were carried out by TEM (Fig. 6). In the as-extruded sample, the spherical intermetallic particles have an average size of ~216 nm. The average size of spherical particles is a little larger with a value of ~275 nm in the peak-aged sample, The spherical particles were identified β-Mg_5RE phase ($F\bar{4}3m$, a=2.33 nm [7]) with XRD (Fig. 2). The selected-area diffraction (SAD) patterns (Fig. 6d) taken from region A (Fig. 6c) indicates the existence of another phase. In this pattern, extra diffraction spots are evenly arranged between directed spot and $(0002)_\alpha$ fundamental spot along the $[0001]_\alpha$. This indicates that the rod-like shaped precipitate is the 14H-type LPSO phase. The XRD results (Fig. 2) demonstrated that some 14H-type LPSO precipitates formed during annealing at 400 °C and 450 °C. The formation of 14H-LPSO phase during high temperature annealing may contribute to a good stability of grain size.

In addition to the β (Mg_5RE) and 14H-type LPSO phases, a fine lamellar precipitate are observed in the extruded samples with and without T5 treatment (Fig. 6a and Fig. 7). These fine lamellar precipitates are of over 500 nm in length and less than 2 nm in thickness. SAD patterns show that streaks are visible along the $[0001]_\alpha$ direction at the $(0000)_\alpha$ and the $\{10\bar{1}0\}_\alpha$ positions (indicated by white arrows in Fig. 7b and Fig. 7d). These diffraction patterns indicate that the habit plane of the fine lamellar precipitate is parallel to the basal plane of Mg matrix. The TEM micrographies (Fig. 7c) observed along the $[11\bar{2}0]_\alpha$ show that β' phase precipitates uniformly distribute in the matrix. The corresponding diffraction spots located at $1/4(10\bar{1}0)_\alpha$, $1/2(10\bar{1}0)_\alpha$, $3/4(10\bar{1}0)_\alpha$ are

indicated by white arrowheads in Fig. 7d. Based on the characteristics of this SAD pattern, β' phase with a bco structure is identified in the sample with T5 treatment.

3.2 Mechanical properties

The tensile properties of the as-extruded and extruded-T5 samples at room temperature and at elevated temperatures are summarized in Table 1. After ageing, both the 0.2% proof stress (YS) and ultimate tensile strengths (UTS) increased substantially, but the ductility increases marginally from 3.8% to 4.1%. The extruded-T5 sample has a UTS of 473 MPa and a YS of 373 MPa at room temperature. With the increase in the test temperature, both the YS and UTS decrease, while the ductility increases. The yield stress is above 340 MPa at 200 °C and above 310 MPa at 250 °C: indicating the good heat resistance of this alloy. The as-extruded sample has a yield stress of 290 MPa at 200 °C and 268 MPa at 250 °C. Below 250 °C the mechanical properties decrease quite slowly with increasing the test temperature. In contrast, above 250 °C the YS and UTS drop rapidly. For extruded-T5 sample, the YS reduces from 316 MPa to 212 MPa with the test temperature raising to 300 °C, while the ductility increases from 6.3% to 35.7%. In the as-extruded sample, the YS is only 172 MPa, while the ductility is 54.4% at 300 °C.

4. Discussion

Table.2 summarizes the mechanical properties of other Mg-RE alloys with similar chemical compositions to the present alloy. Compared with other Mg-RE alloys, the ductility of extruded-T5 alloy is not very high. However, it has a higher 0.2% proof stress than the majority of alloys (Table 2) [3–8]. The YS is only lower than that of

Mg-14Gd-0.5Zr [9] and Mg-10Gd-5.66Y-1.62Zn-0.65Zr alloys [10]. The high YS of the present alloy is attributable to the basal-texture, grain refinement, LPSO phase and the fine dense β' phase. The details about strengthening mechanisms will be discussed below.

4.1 Strengthening by the basal-fiber texture

As shown in Fig. 5a, the dynamic recrystallization occurs in the α-Mg matrix during hot extrusion. The average size of recrystallized grains is ~2.5 μm following extrusion. The high amount of RE elements in this alloy facilitates the formation of LPSO and Mg_5RE phases. As a result, the dislocations pile up at the interfaces between LPSO or Mg_5RE phases and Mg matrix. The dislocation pileup increases the dislocation density and possibly results in the formation of subgrain [19]. Since subgrain coalescence is one of the mechanisms of recrystallization nucleation [20], the dynamic recrystallization would occur when the dislocation density exceeds a critical value. The fine equiaxed grains that formed with texture during hot extrusion influence the mechanical properties.

Due to the textures shows in Fig. 5b, the Schmid factor of (0001) <11$\bar{2}$0> basal slip is extremely small when the tensile load parallels to ED. In magnesium alloys, (0001) <11$\bar{2}$0> basal slip is the dominant deformation mode at room temperature. A microstructure with the basal texture can strengthen the matrix by impeding the activation of basal slip. However, the intensity of basal texture is considerably weaker in the present alloy than that in the conventional wrought Mg alloys such as AZ31 alloy [21]. The weak texture is attributed to the additions of RE. Recently it was reported that the addition of RE such as Ce, Gd and Y weakened the basal texture and improved the deformation

homogeneity [21–23]. The weak basal texture caused by the addition of RE is also beneficial for the improvement of ductility [24, 25].

4.2 Strengthening by fine grains, LPSO phase and fine lamellar precipitates

Before annealing treatment, the average grain size of extruded sheet is ~2.5 μm. The grain boundary strengthening can be estimated using the Hall-Patch relation $\sigma_y = \sigma_0 + k_y d^{1/2}$ (σ_y is the yield strength, σ_0 is the intrinsic stress, k_y is the proportionality constant, d is the grain size). The hot extrusion leads to the refinement of grains and increment of grain boundaries. The yield strength has an inverse proportion to the grain size and to the fraction of grain boundary. According the previous work [3], the grain boundary strengthening in the extruded-T5 sample is the main strengthening mechanism to improve the experimental yield strength. Since the cast-T6 sample has a bigger grain size, the contribution of grain boundary is less than that in the extruded-T5 sample. Thus, the fine grains effectively contribute to the improvement of mechanical properties of the present alloy. The Mg alloy has a stable grain size, since the average grain size is ~8 μm after annealing at 450 °C for 72 h (Fig. 3e). The reasons for the fine microstructure are attributed to the presence of β and 14H-LPSO phases at the grain boundaries. One reason for the fine grains is the dynamic precipitation of β phase, which forms at the grain boundaries during hot-extrusion. The neodymium addition generally promote a large volume fraction of β phases in Mg-Gd-Nd alloys [26]. These β particles pin the grain boundaries and hinder the growth of recrystallized grains. During annealing treatment at high temperatures 400 °C or 450 °C, the majority of β particles dissolves into the α-matrix, meanwhile, the residual β particles coarsen (Fig. 3 and Fig. 4).

Consequently, the resistance to the grain growth reduces. The grains coarsen gradually. Another reason for the fine grain size is the 14H-LPSO phase. The LPSO phase enhances the refinement of crystallized grain during hot-extrusion by inducing stress concentrations.

Compared with Mg matrix, LPSO phase is a hard phase. Thus, the stress concentration is due to the incompatible deformation which occurs at the interface between the LPSO phase and Mg matrix. Compared with the β phase, the finely dispersed LPSO phase has a better thermal stability, since it remains stable after annealing at high temperatures (Fig. 3d and e, Fig. 4e). After annealing, the peaks of LPSO phase still exist while the peaks of Mg_5RE disappear (Fig. 2c and d). The intensity of LPSO peaks in Fig. 2d is also stronger than that in Fig. 2c, indicating that the annealing treatment at 450 °C may result in the formation of more LPSO phases. The previous studies [16, 29] show that, 14H-LPSO phase forms and grow at temperatures >350 °C due to a decrease in stacking fault energy. Most Mg_5RE phases dissolves at temperatures above 400 °C, the content of alloying elements in the Mg matrix increases; and new LPSO structures form during annealing process. The existing LPSO phase remains stable during annealing treatment. Thus, the volume fraction of LPSO phases probably increases. LPSO phase normally possesses a relative large aspect ratio and distributes along grain boundaries. They act as the main strengthening phase instead of Mg_5RE in this alloy when the temperature exceeds 400 °C.

14H-LPSO phase has a rod-like shape. It has an orientation relationship with α-Mg matrix $(0001)_{14H\text{-}LPSO}$ // $(0001)\alpha$, $[01\bar{1}0]_{14H\text{-}LPSO}$ // $[11\bar{2}0]_{\alpha}$ [27]. This phase has a plate-like interface which parallels to $(0001)_{LPSO}$, and its dominant deformation mode proceeds by

(0001) <11$\bar{2}$0> basal slip [17, 18]. Since the majority of 14H-LPSO precipitates parallel to ED, their $(0001)_{LPSO}$ is also parallel to ED. If the tensile load is parallel to the ED, the critical resolved shear stress (CRSS) of basal slip is very large as the Schmid factor for the basal slip is negligible. The basal slip of 14H-LPSO phases is then effectively suppressed. Based on the deformation mechanism of 14H-LPSO and its volume fraction, 14H-LPSO precipitates could be much better to improve the strength via a short-fiber strengthening mechanism [24]. When the tensile load exceeds CRSS of the basal slip, the shear deformation always occurs across the LPSO phases and kink bands form in the LPSO phase. In a previous study [34], it is shown that once the kink angle increases to a critical value, microcracks nucleate at the kink boundaries and propagate along the basal plane of kink band in the LPSO phase. However, its propagation could be restrained, by the basal planes of the next kink band would deflected the crack from the propagation direction. The cleavage of each kink band would occur and microcracks would not cross easily into the neighboring kind band. The LPSO phase effectively hinder the motion of microcracks. The microcracks nucleate at kink boundaries in the LPSO phase, but there are no voids or microcracks at the coherent interface between LPSO phase and Mg matrix. The stability of this interface is beneficial for the strength and ductility of this alloy. In previous studies [15, 16, 24], it was shown that the plastic deformation, such as extrusion, is effective in strengthening the alloys with LPSO phase. The reasons are that the extrusion brings about the refined Mg grains and uniformly dispersed LPSO phase. It is an attractive way to prepare heat-resistant Mg alloy through precipitation of large volume fraction of aligned LPSO phases.

The fine lamellar precipitates (Fig. 6a and Fig. 7) contribute to strength of the alloy.

The clustering of fine lamellar precipitates is found in both as-extruded samples and samples aged at 200 °C for 72 h. Similar reflection streaks to this investigation (Fig. 7b and 6d) were also observed in Mg-Gd-Zn [28, 29] and Mg-Gd-Y-Zn-Zr [10] alloys. These precipitates were identified as γ' phase [28] or stacking faults [29]. According to the previous investigations [28, 30, 31, 34], these plates precipitate on the basal planes with a uniform distribution, which provide effective barriers to the motion of non-basal dislocations and the twin nucleation. Thus, these particles contribute to improvement of the tensile and creep properties of Mg alloys [28, 30, 31, 34].

4.3 Strengthening by solid solution and β' phase

Solid solution strengthening is another contribution to improve the mechanical properties in both the as-extruded and extruded-T5 samples. The atomic radius is 0.180 nm for Gd, 0.212 nm for Y, 0.206 nm for Nd, 0.133 nm for Zn and 0.160 nm for Mg, respectively. Replacing a Mg atom by a RE atom leads to a positive misfit (0.125 for Gd, 0.325 for Y, 0.288 for Nd) and a compression strain, while replacing a Mg atom by a Zn atom causes a negative misfit (-0.169) and an tensile strain. In the matrix, the misfit by different atoms leads to lattice distortion. Both the RE and Zn atoms may act as an effective barrier to the motion of gliding dislocations [28]. The contribution caused by solid solution strengthening decreases due to that the formation of precipitates consumes the solutes in the matrix during aging treatment. Obviously, the contribution from solid solution strengthening in the cast-T6 sample is less than that in the cast-T4 sample [3].

After hot extrusion, due to that the grains were refined and more fine particles were dynamically precipitated, more contributions to the strength are caused by grain boundary

strengthening and precipitate strengthening. As a result, compared with the samples without hot extrusion, the contribution proportion of its solid solution strengthening to the improvement of alloy strength reduces.

A high dislocation density facilitates the nucleation of precipitates during ageing treatment [9]. Due to the high density of dislocations induced by both LPSO and β phases during hot extrusion, a considerable amount of nano-scale β' phase precipitate after ageing treatment at 200 °C (Fig. 7d). The previous results [32, 33] showed that the orientation relationship between the β' phase and α-Mg matrix is $(001)_{\beta'}$ // $(0001)_{\alpha\text{-Mg}}$ and $[100]_{\beta'}$ // $[2\bar{1}\bar{1}0]_{\alpha\text{-Mg}}$. The β' phase precipitates on the prismatic planes parallel to $\{2\bar{1}\bar{1}0\}_{\alpha\text{-Mg}}$. They distribute in a dense triangular array in the α-matrix providing the effective obstacles to basal dislocation slip. The maximum solvus temperature of the β' phase is reported to be less than 300 °C [33], the β' phase contribute to strengthening during tensile test at 250 °C [32, 33].

5. **Conclusions**

A magnesium alloy Mg-11Gd-4.5Y-1.5Zn-1Nd-0.5Zr (wt.%) with high strength and heat resistance has been prepared successfully by hot extrusion and subsequent ageing treatment. The following conclusions can be drawn:

1. The present alloy exhibits excellent mechanical properties with UTS of 473 MPa, YS of 373 MPa and elongation to failure of 4.1% at room temperature. The YS is still above 340 MPa at 200 °C and above 310 MPa at 250 °C.
2. The as-cast alloy contains α-Mg solid solution, Mg_5RE, Mg_3RE and $Mg_{12}REZn$ phases. After T4 treatment, only $Mg_{12}REZn$ phase and a small amount of Mg_5RE

exist. In the as-extruded alloy, Mg_3RE phase does not appear. After the annealing treatment above 400 °C, a majority of the Mg_5RE phase dissolve, but the $Mg_{12}REZn$ phase still exists and precipitates.

3. This alloy possesses an good thermal stability. The average grain size remains ~8 μm after annealing at 450 °C for 72 h. The excellent thermal stability is attributed to the Mg_5RE phase which strengthens the alloy up to 400 °C and the LPSO phase which strengthens the alloy above 400 °C.
4. 14H-LPSO phase facilitates the grain refinement during hot-extrusion. After the hot-extrusion, the aligned 14H-LPSO phases improve the mechanical properties of the alloy via a short-fiber strengthening.
5. The solid solution, basal-fiber texture, dispersed fine lamellar precipitates and the fine recrystallized grains contribute to strengthen the alloy. The β' phase which forms during ageing treatment improves the YS by ~50 MPa and the UTS by ~100 MPa at room temperature.

Acknowledgements

This work is supported by the National Key Technologies R&D Program (2012BAE01B04，2011BAE22B01, 2011A080403008, 201001C0104669453)

References

[1] P. Vostrý, B. Smola, I. Stulíková, F. von Buch and B. L. Mordike, Phys. Stat. Sol. (a) 175 (1999) 491–500.

[2] N. Hort, Y. Huang, D. Fechner, M. Störmer, C. Blawert, F. Witte, C. Vogt, H. Drücker, R. Willumeit, K. U. Kainer, F. Feyerabend, Acta BioMater. 6 (2010) 1714–1725.

[3] S. M. He, X. Q. Zeng, L. M. Peng, X. Gao, J. F. Nie, W. J. Ding, J. Alloys Compd. 427 (2007) 316–323.

[4] I. A. Anyanwu, S. Kamado, Y. Kojima, Mater. Trans. 42 (2001) 1206–1211.

[5] T. Itoi, T. Suzuki, Y. Kawamura, M. Hirohashi, Mater. Trans. 51 (2010) 1536–1542.

[6] X. L. Hou, Z. Y. Cao, L. Zhao, L. D. Wang, Y. M. Wu, L. M. Wang, Mater. Des. 34 (2012) 776–781.

[7] X. B. Liu, R. S. Chen, E. H. Han, J. Alloys Compd. 465 (2008) 232–238.

[8] R. Wang, J. Dong, L. K. Fan, P. Zhang, W. J. Ding, Trans. Nonferrous Met. Soc. China. 18 (2008) 189–193.

[9] R. G. Li, J. F. Nie, G. J. Huang, Y. C. Xin, Q. Liu, Scripta Mater. 64 (2011) 950–953.

[10] T. Homma, N. Kunito, S. Kamado, Scripta Mater. 61 (2009) 644–647.

[11] J. F. Nie, Scripta Mater. 48 (2003) 1009–1015.

[12] Y. Negishi, T. Nishimura, M. Kiryuu, S. Kamado, Y. Kojima, R. Ninomiya, J. Japan. Inst. Light Metals. 45 (1995) 57-63.

[13] Y. Kawamura and M. Yamasaki, Mater. Trans. 48 (2007) 2986–2992.

[14] Y. Kawamura, K. Hayashi, A. Inoue, T. Masumoto, Mater. Trans. 42 (2001) 1172–1176.

[15] S. Yoshimoto, M. Yamasaki, Y. Kawamura, Mater. Trans. 47 (2006) 959–965.

[16] M. Yamasaki, T. Anan, S. Yoshimoto, Y. Kawamura, Scripta Mater. 53 (2005) 799–803

[17] K. Hagihara, N. Yokotani, Y. Umakoshi, Intermetallics. 18 (2010) 267–276.

[18] K. Hagihara, N. Yokotani, A. Kinoshita, Y. Sugino, H. Yamamoto, M. Yamasaki, Y. Kawamura and Y. Umakoshi, Mater. Res. Soc. Symp. Proc. Vol. (2009) 1128-1134.

[19] K. Hagihara, A. Kinoshita, Y. Sugino, M. Yamasaki, Y. Kawamura, H. Y. Yasuda, Intermetallics. 18 (2010) 1079–1085.

[20] F. J. Humphreys, M. Hatherly . Recrystallization and related annealing phenomena. 2nd ed. UK: Galliard; 2004.

[21] N. Stanford, D. Atwell, A. Beer, C. Davies and M.R. Barnett, Scripta Mater. 59 (2008) 772-775

[22] N. Stanford, D. Atwell, M. R. Barnett, Acta Mater. 58 (2010) 6773–6783.

[23] J. Bohlen, M. R. Nürnberg, J. W. Senn, D. Letting, S. R. Agnew, Acta Mater. 55 (2007) 2101-2112.

[24] K. Hagihara, A. Kinoshita, Y. Sugino, M. Yamasaki, Y. Kawamura, H.Y. Yasuda,Y. Umakoshi, Acta Mater. 58 (2010) 6282–6293.

[25] Y. Yoshida, L. Cisar, S. Kamado, Y. Kojima, Mater Trans. 44 (2003) 468–475.

[26] P. J. Apps, H. Karimzadeh, J. F. King, G. W. Lorimer, Scripta Mater. 48 (2003) 1023–1028.

[27] Y. M. Zhu, A. J. Morton, J. F. Nie, Acta Mater. 58 (2010) 2936–2947.

[28] J. F. Nie, K. Oh-ishi, X. Gao, K. Hono, Acta Mater. 56 (2008) 6061–6076.

[29] M. Yamasaki, M. Sasaki, M. Nishijima, K. Hiraga,Y. Kawamura, Acta Mater. 55 (2007) 6798–6805.

[30] M. Suzuki, T. Kimura, J. Koike, K. Maruyama, Scripta Mater. 48 (2003) 997–1002

[31] J. F. Nie, X. Gao, S. M. Zhu, Scripta Mater. 53 (2005) 1049–1053

[32] J. F. Nie and B. C. Muddle, Acta Mater. 48 (2000) 1691–1703.

[33] J. F. Nie and B. C. Muddle, Scripta Mater. 40 (1999) 1089–1094.

[34] X. H. Shao, Z. Q. Yang, X. L. Ma, Acta Mater. 58 (2010) 4760–4771.

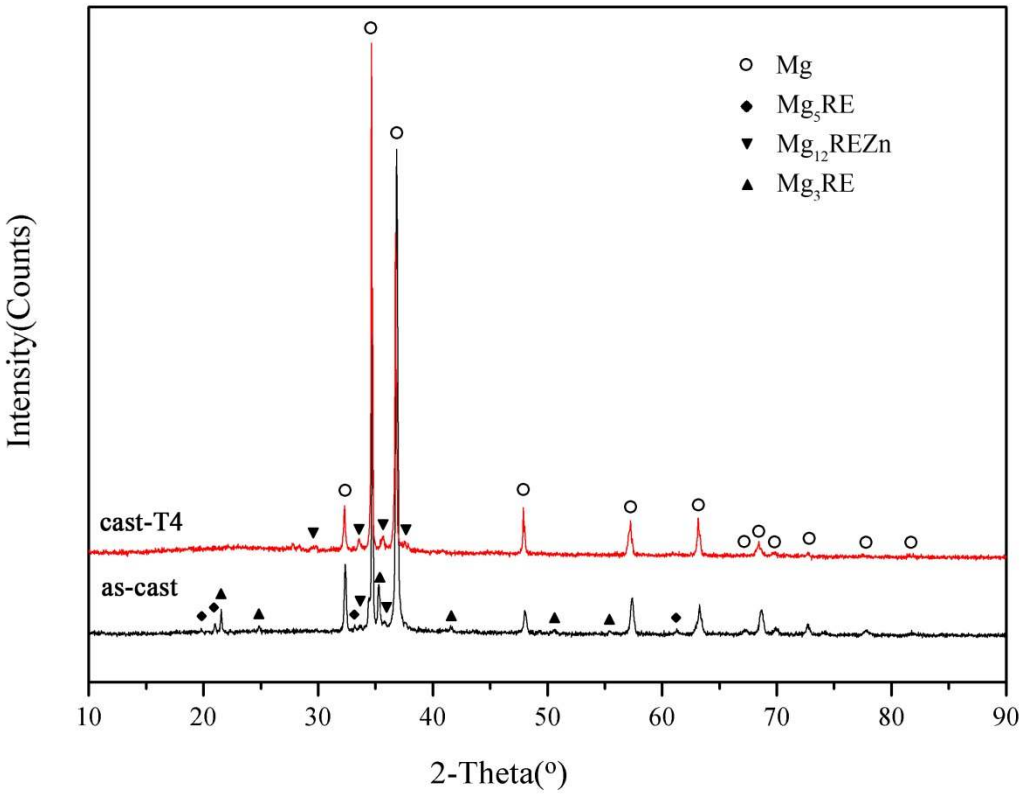

Fig.1. X-ray diffraction patterns of as-cast and cast-T4 samples

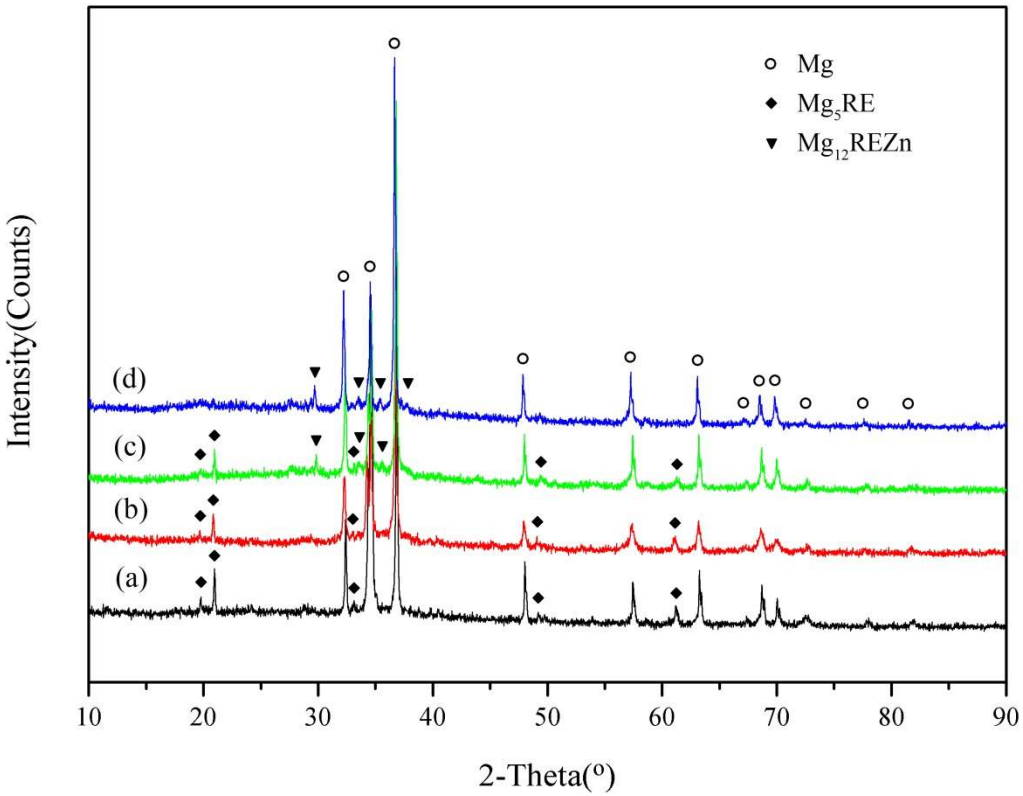

Fig.2. X-ray diffraction patterns of as-extruded and extruded-T5 treated samples: (a) as-extruded sample; (b) peak-aged at 200°C; (c) annealing at 400°C for 72 hours; (d) annealing at 450°C for 72 hours.

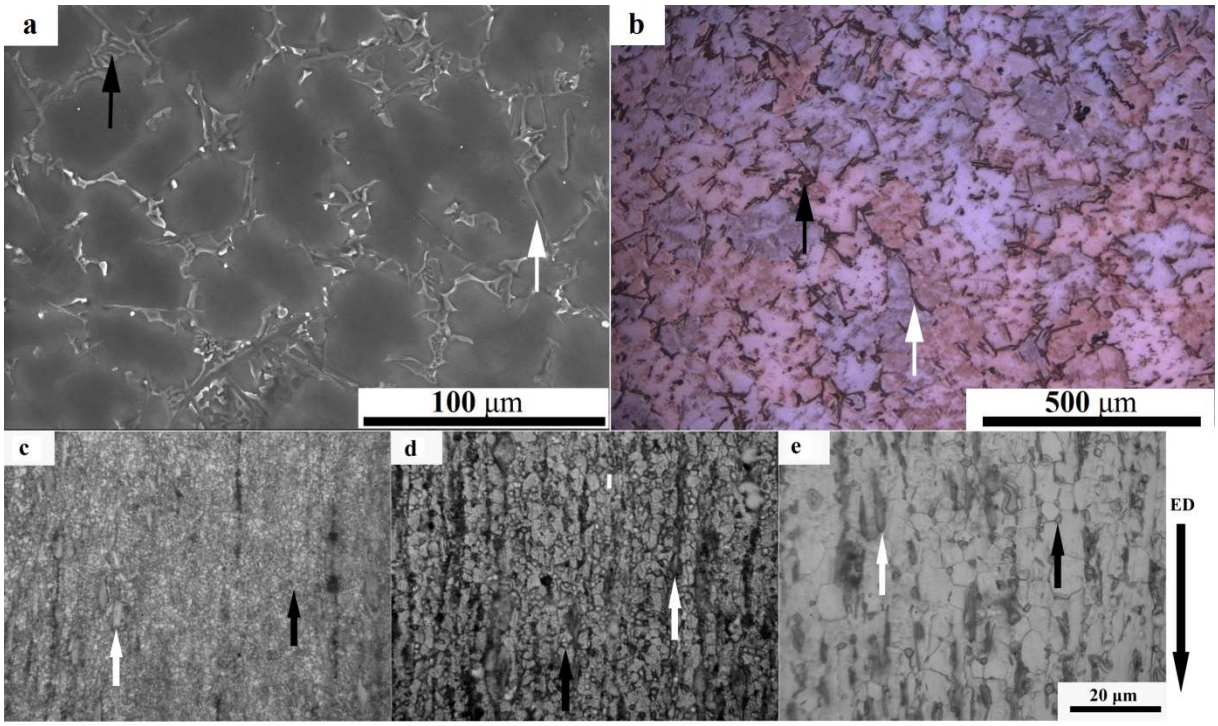

Fig.3. Variations of microstructures of the samples at different states, (a) SEM image of as-cast sample; (b) OM image of cast-T4 sample; (c) OM image of as-extruded sample; OM images of as-extruded samples with annealing treatment at (d) 400°C and (e) 450°C for 72h.

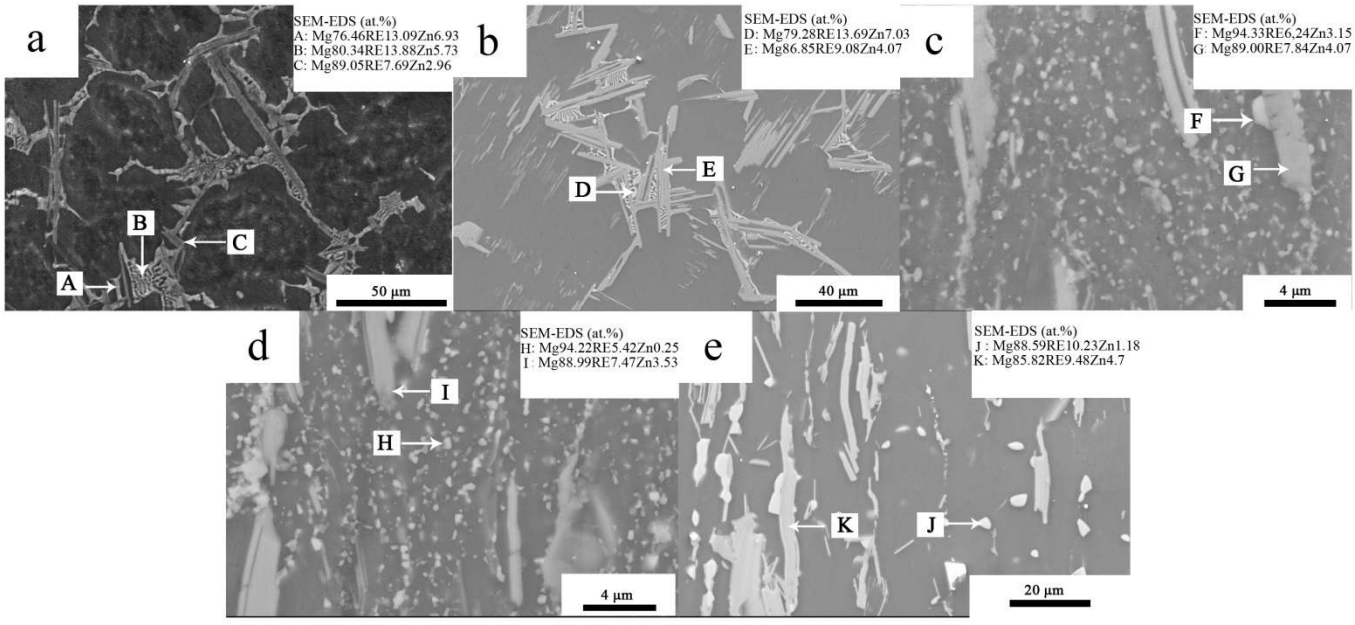

Fig.4. SEM images of the samples at different states,(a) as-cast sample; (b)cast-T4 sample; (c) as-extruded sample; (d) extrueded-T5 sample; (e)as-extruded sample with annealing treatment at 450℃ for 72 hours. The insets in these images are the corresponding SEM-EDS results of particles marked with A-K.

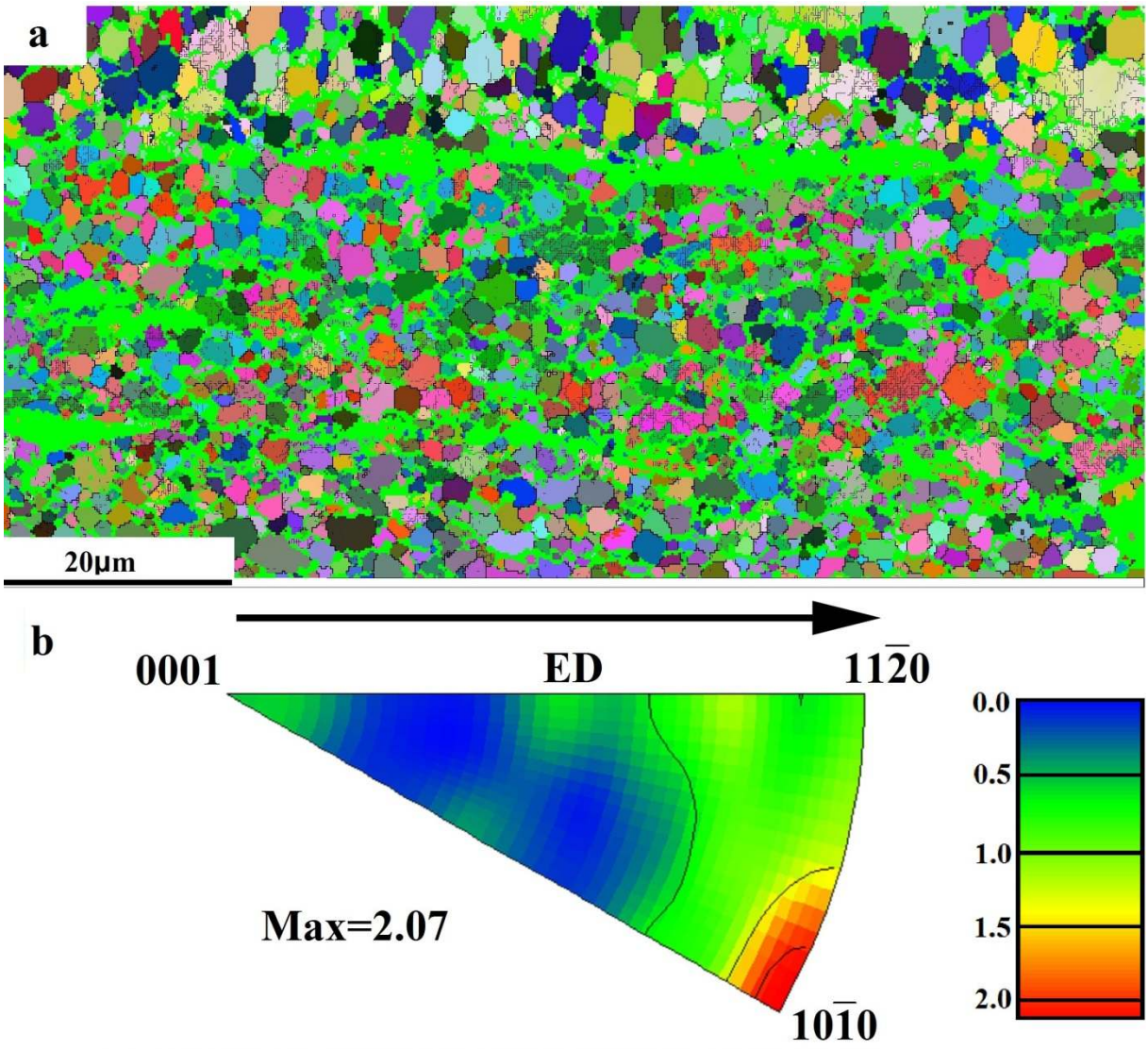

Fig.5. EBSD IPF image (a) of as-extruded sample obtained from the longitudinal section along the direction of extrusion(ED). Corresponding inverse pole figures (b) derived from the matrix grains.

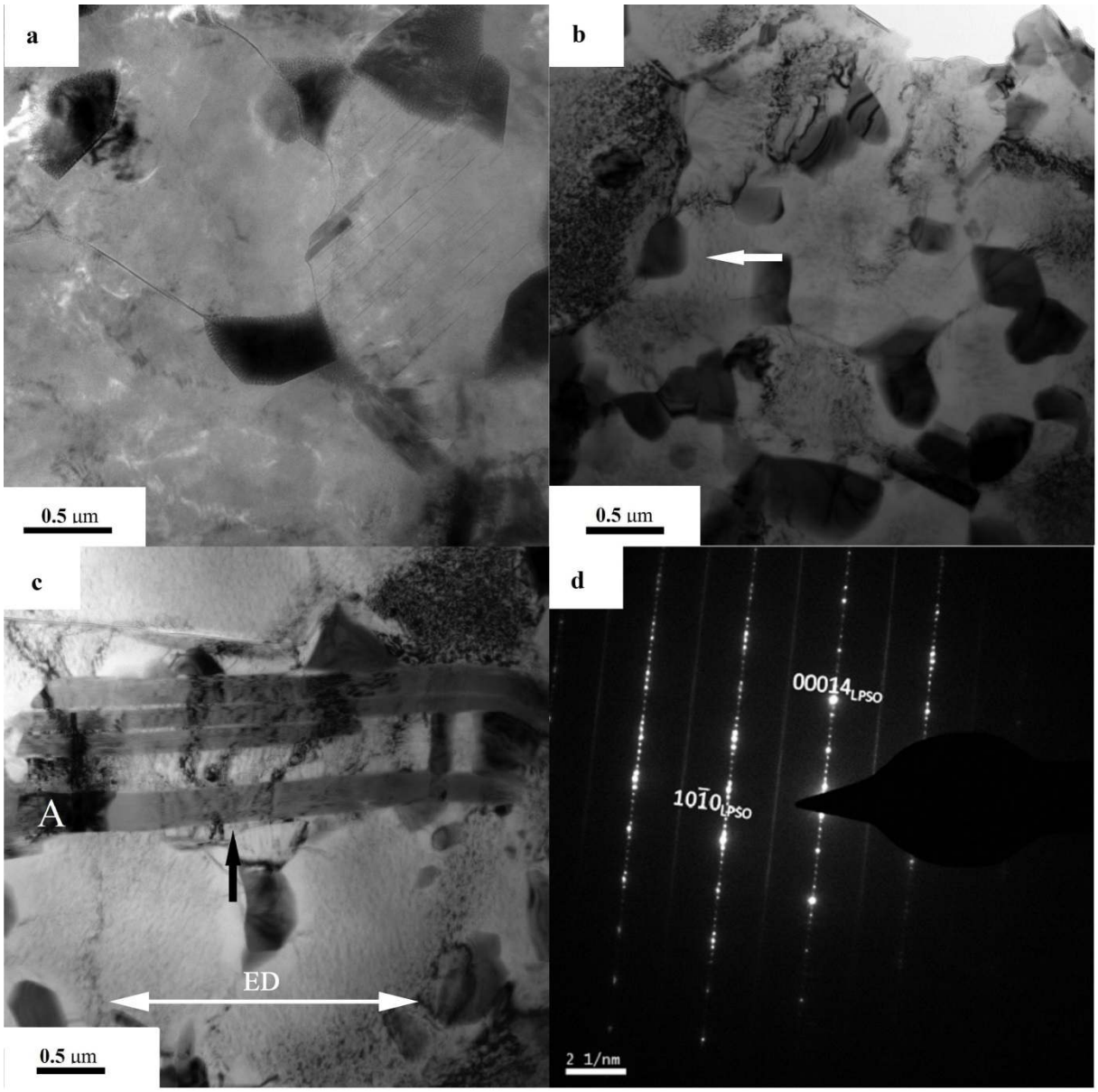

Fig.6. TEM bright-field (BF) image showing intermetallic particles around the grain boundaries in the as-extruded sample (a); TEM BF images of intermetallic particles and LPSO phases (b and c) in the T5-treated sample, and corresponding SEAD patterns (B//$[11\bar{2}0]_{\alpha}$) (d).

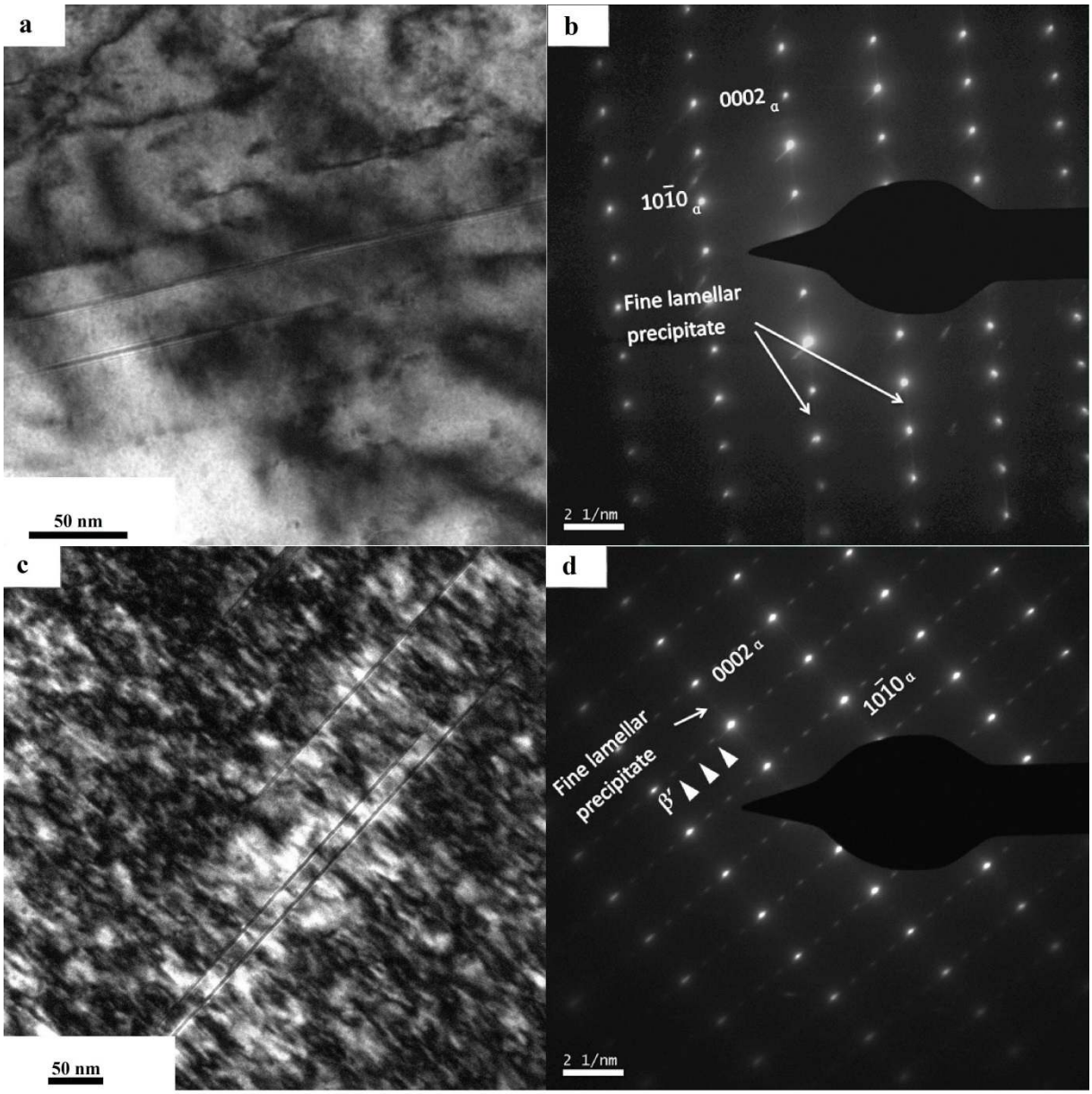

Fig.7. TEM BF image showing fine lamellar precipitates inside the α-Mg grain and corresponding SAED patterns (B// [11$\bar{2}$0]α) in the as-extruded sample (a and b); TEM BF image of fine lamellar precipitates and β' phases inside the α-Mg grain and corresponding SAED patterns (B// [11$\bar{2}$0]α) in the T5-treated sample(c and d).